UNIVERSITÀ DEGLI STUDI DI PADOVA

Dipartimento di Fisica e Astronomia "Galileo Galilei"

Corso di Laurea in Fisica

Final dissertation

Charge reconstruction from photomultiplier signals

for the JUNO experiment

Thesis supervisor

Alberto Garfagnini

Thesis co-supervisor

Katharina von Sturm

Candidate

Camilla Forza

Academic Year 2020-2021

Contents

Abstract

Jiangmen Underground Neutrino Observatory (JUNO) is a multi-purpose neutrino experiment under construction in South China. It will have 20 ktons of highly transparent liquid scintillator contained in an acrylic sphere surrounded by 18000 20" PMTs and 25000 3" PMTs, providing an energy resolution better than 3% at 1 MeV. JUNO is expected to be able to resolve the neutrino mass hierarchy, significantly improve accuracy of the solar oscillation parameters and make a significant impact on other neutrino physics domains. The amount of light emitted in the liquid scintillator is proportional to the deposited energy. The light is transformed into photoelectrons which are amplified and measured by the PMTs. In order to characterize and optimize the electronic system response of PMTs, a small JUNO mock-up has been constructed at the Laboratori Nazionali di Legnaro (LNL) and calibration operations are ongoing. In this thesis, a procedure for the charge reconstruction from PMTs signals has been developed and tested reconstructing data from a 137 Cs source. Afterwards, single photon measurements from a LED source have be studied and the reconstructed charge spectrum has enabled further studies on PMT gain calculations. Finally, in order to select the same gain for all PMTs, an analysis of the gain as a function of the PMT bias voltage of the PMT has been performed and detailed results are presented in this thesis.

Chapter 1

Introduction

1.1 The JUNO Experiment

The Jiangmen Underground Neutrino Observatory (JUNO) [1] is a large liquid scintillator (LS) neutrino experiment whose aim is to challenge important issues of neutrino physics and astrophysics. JUNO is a 20 kton liquid scintillator detector located 700 m underground in a laboratory in South of China. The experiment main goal is detecting reactor antineutrinos to solve the Neutrino Mass Ordering (NMO) problem, providing a NMO determination at 3-4 σ significance after six years of data taking. Moreover, JUNO will perform high precision measurements of neutrino the oscillation parameters: $\sin^2 \theta_{12}$, Δm_{21}^2 and $|\Delta m_{32}^2|$ to subpercent level. The experiment will also study neutrinos generated by core-collapse supernovae, solar neutrinos, atmospheric neutrinos and geoneutrinos [1]. The JUNO experiment is located under the Dashi hill, 43 km Southwest of Kaiping city, next to Jiangment city. A map of the region is provided in Fig. 1.1. The experimental site has been located equally far from the Yangjiang Nuclear Power Plant (NPP) and the Taishan NPP (approximately 53 km), while the Daya Bay nuclear complex is 215 km away from JUNO. All distances are listed in Tab. 1.1. The detector position has been properly chosen in order to optimize the sensitivity to the mass ordering, being the main purpose of the experiment.

Figure 1.1: A map showing the location of the JUNO detector.

To minimize the systematics due to the reactor anti-neutrino beam uncertainty, a reference detector will be operated at a few meters from on of the Thaishan reactor core. The Thaishan Antineutrino Observatory (TAO) [2] is a liquid scintillator detector specifically

Cores	YJ-1	YJ-2	YJ-3	YJ-4	YJ-5	YJ-6	TS-1	TS-2	DYB	HZ
Power (GW)	2.9	2.9	2.9	2.9	2.9	2.9	4.6	4.6	17.4	17.4
Baseline (km)	52.74	52.82	52.41	52.49	52.11	52.19	52.77	52.64	215	265

Table 1.1: Distances of Nuclear Power Plants (NPPs) from the JUNO detector.

designed to achieve precise measurements of the reactor antineutrinos spectrum, having a key role in the NMO determination.

1.2 Neutrino physics with JUNO

One of the still unanswered issues in neutrino physics is the NMO determination [3]. In the NMO quest, which can be investigated with different experimental techniques, JUNO is unique investigating the probability of survival of reactor antineutrinos produced by nuclear reactors 53 km away from the experimental site, with negligible from matter in the definition of oscillation parameters. The three flavour eigenstates neutrinos ν_e, ν_μ, ν_τ can be determined as coherent superpositions of the three mass eigenstates ν_i, (i=1,2,3), by the action of U:

$$\begin{pmatrix} \nu_e \\ \nu_\mu \\ \nu_\tau \end{pmatrix} = \begin{pmatrix} U_{e1} & U_{e2} & U_{e3} \\ U_{\mu1} & U_{\mu2} & U_{\mu3} \\ U_{\tau1} & U_{\tau2} & U_{\tau3} \end{pmatrix} \cdot \begin{pmatrix} \nu_1 \\ \nu_2 \\ \nu_3 \end{pmatrix} \tag{1.1}$$

Where U is 3x3 matrix called Pontecorvo-Maki-Nakagawa-Sakata (PMNS) [4] matrix describing the flavour oscillation of neutrinos, possible only if neutrinos have non-null mass. A parametrization of the PMNS matrix can be done in terms of the three angles θ_{13}, θ_{23}, θ_{12} and the CP phase δ_{CP}. The reaction used to detect reactor antineutrinos in JUNO experiment is the Inverse Beta Decay (IBD) where an electron antineutrino interacts with a proton of the liquid scintillator forming a neutron and a positron,

$$\bar{\nu}_e + p \longrightarrow n + e^+ \ . \tag{1.2}$$

The positron annihilates into two 511 keV gamma-rays, while the neutron thermalizes and it is finally captured on a proton (99%) or carbon (1%) after 200 μs on average. The neutron signal is detected after a delayed time compared to the gamma-rays.

The survival probability of $\bar{\nu}_e$ in vacuum can be written as:

$$P_{ee} = 1 - \sin^2 2\theta_{13} \cdot (\cos^2 \theta_{12} \sin^2 \Delta_{31} + \sin^2 \theta_{12} \sin^2 \Delta_{32}) - \sin^2 2\theta_{12} \cdot \cos^4 \theta_{13} \sin^2 \Delta_{12}$$

Where $\Delta_{ij} = \frac{\Delta m_{ij}^2 L}{4E_\nu}$ and the dependence on the PMNS matrix parameters is evident. The survival probability depends also on the difference between the squared mass eigenvalues Δm_{ij}^2 and on the distance L, calculated from the first measurement of the flavour of antineutrinos and the detecting point. Using the approximation $\Delta m_{32}^2 \approx \Delta m_{31}^2$, the probability becomes:

$$\begin{aligned} P_{ee} =& 1 - \cos^4 \theta_{13} \sin^2 2\theta_{12} \sin^2 \Delta_{21} - \sin^2 \theta_{13} \sin^2 |\Delta_{31}| \\ & - \sin^2 \theta_{12} \sin^2 2\theta_{13} \sin^2 \Delta_{21} \cos 2|\Delta_{31}| \\ & \pm (\sin^2 \theta_{12}/2) \cdot \sin^2 2\theta_{13} \sin^2 2\Delta_{21} \sin^2 2|\Delta_{31}| \end{aligned} \tag{1.3}$$

The last term of the formula presents two possibilities, plus or minus, which are strictly related to the mass ordering. The positive solution is linked to the Normal Ordering (NO)

and the negative refers to the Inverse Ordering (IO). The discriminator of the NMO make use of the least chi-squared method and has this form:

$$\Delta\chi^2_{MO} = |\chi^2_{min}(NO) - \chi^2_{min}(IO)| \quad , \tag{1.4}$$

where the chi-squared function is specifically defined for the purpose. It is expected to obtain $\chi^2 = 10$ which corresponds to a significance of 3σ after 6 years of data taking [1]. The JUNO experiment will also study the effects of the so called solar and atmospheric oscillations simultaneously being the first experiment to do it. In fact, precise values of neutrino oscillation parameters will be obtained measuring the oscillated reactor antineutrino spectrum.

1.3 Detector design overview

The JUNO detector, shown in Fig. 1.2, is composed by three main parts: the Central Detector (CD), consisting in a liquid scintillator housed in an acrylic vessel, the Water Cherenkov Detector (WCD) and the Top Tracker (TT). These last two detectors form the VETO system of the experiment. JUNO is a very challenging detector because of its giant volume and low background claim, being located 700 m underground and requiring high performances in energy resolution.
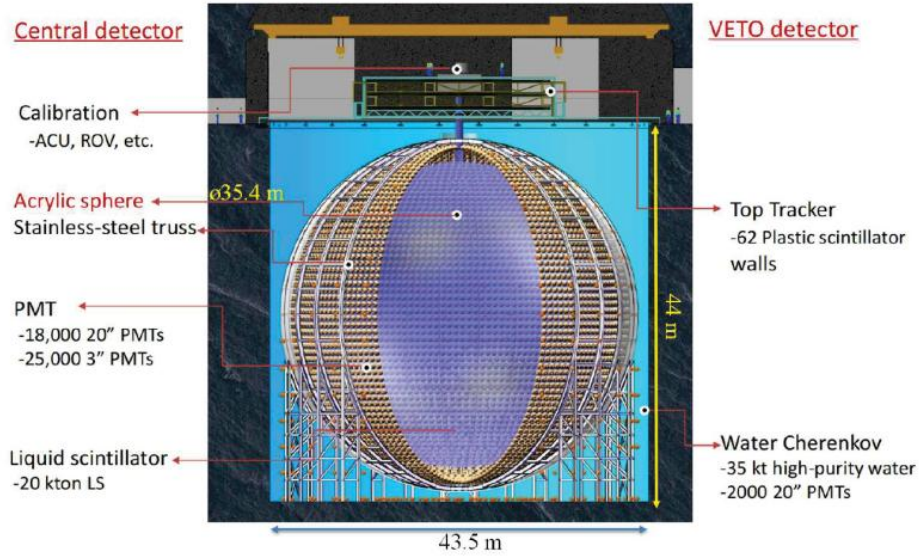

Figure 1.2: Graphical image of the JUNO detector.

The Central Detector is formed by a spherical acrylic vessel of 35.4 m inner diameter and a thickness of 120 mm containing 20 kton of Liquid Scintillator (LS). The effective energy resolution of the CD is ambitiously planned to be $3\%/\sqrt{E(MeV)}$ [5]. The acrylic vessel is made of 265 pieces of spherical acrylic panels using bulk polymerization which guarantees an increase of transparency to scintillator light and a reduction of radioactive background. The transparency of spherical acrylic panels gains a level of transparency >96% in the water, due to the choice regarding the material and the production method. The radioactive background produced by the vessel is mostly given by Thorium and Uranium and the radiopurity of acrylic for these sources achieves the level of <0.5 ppt after the cleaning process. The greater part of LS is Linear Alky Benzene (LAB) which is a straight alkyl chain of 10-13 carbons attached to a benzene ring. Excellent transparency,

high flash point, low chemical reactivity and good light yield are the most crucial properties of the material. The JUNO LS recipe is also made of other two parts: 2.5 g/L of 2.5-diphenyloxazole as the fluor and 3 mg/L p-bis-(o-methylstyryl)-benzene as wavelength shifter. The scintillator light is read by photomultipliers (PMTs) surrounding the vessel in all directions. Two types of PMTs are used in the CD, specifically 17612 20-inch PMTs called "large PMTs" and 25600 3-inch PMTs called "small PMTs". The photocathode coverage for large PMTs is 75.2% and for small PMTs is 2.7% instead. Furthermore, the average photon detection efficiency is 28.7% for the former and >24% for the latter.

The detector is held by a stainless steel structure designed specifically to house the CD and to support the PMTs, the front-end electronics, cables and the anti-geomagnetic field coil. PMTs of the CD are located in the structure facing the inside to detect scintillator light, PMTs of the WCD facing the outside instead. The Main Structure has also been studied to be safe in case of earthquakes. The VETO system fundamentally includes two detectors, the Water Cherenkov Detector (WCD) and the Top Tracker, working together to track particles coming from cosmic rays and environmental radioactivity. These particles compose the greatest part of background crossing the detector and there have been several efforts to reach an efficient background reduction. The WCD, shown in Fig. 1.2, is a cylinder filled with 30 ktons of ultrapure water surrounding the CD, its dimensions are 43.5 m in diameter and 44 m in height. The Cherenkov light, mostly produced by muons crossing the volume, is detected by 2400 20-inch Microchannel Plate Photomultipliers settled on the external surface of the Main Structure. Large volume of water has also another scope that is reducing the noise due to the radioactivity of the surrounding rocks, shielding the gamma background in the CD. Temperature uniformity is claimed to ensure the mechanical stability and it is maintained around 21°C. All these precautions and requests enable the expected muon tagging efficiency of the WCD to reach 99.5%. The Top Tracker (TT) has been placed on the top of the WCD and it is basically composed by several scintillator strips grouped together to form TT modules. The signal travelling in the wavelength shifting fiber, placed inside each scintillator strip, is read by PMTs from both sides. A layer is built combining TT modules and two layers one above the other, rotated by 90°, create a TT wall. The structure of the detector can be seen in Fig. 1.3. The expected efficiency for the TT module is $(98.0 \pm 0.5)\%$.
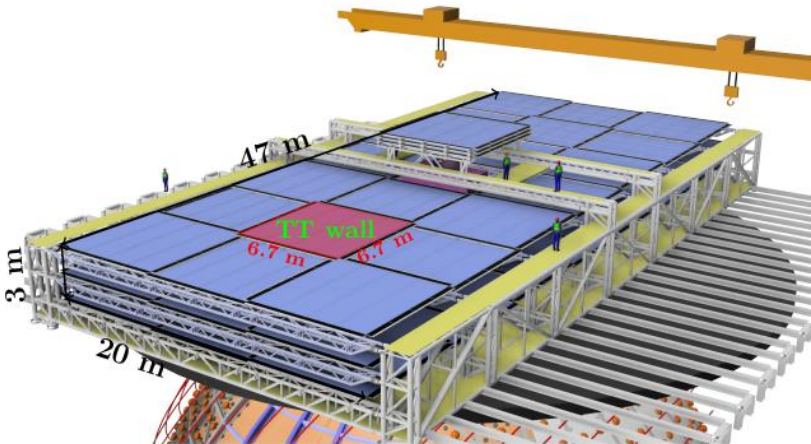

Figure 1.3: Graphical image of the JUNO Top Tracker.

4

Chapter 2

The JUNO test facility at LNL

An high reliability of the Front-End electronics is an important requirement for JUNO in order to have good sensibility and enough statistic to measure NMO. The reason can be found on the fact that all PMTs and the electronic components around the Central Detector will not be reachable after the underwater installation. The required tolerance for PMTs is 0.5% defective channels over 6 years of data taking and for the purpose a complete characterization and optimization of the system response has been developed. A small mock-up of JUNO has been constructed at the Laboratori Nazionali di Legnaro (LNL) in order to study the electronic system response. A drawing of the JUNO test facility is shown in Fig. 2.1.
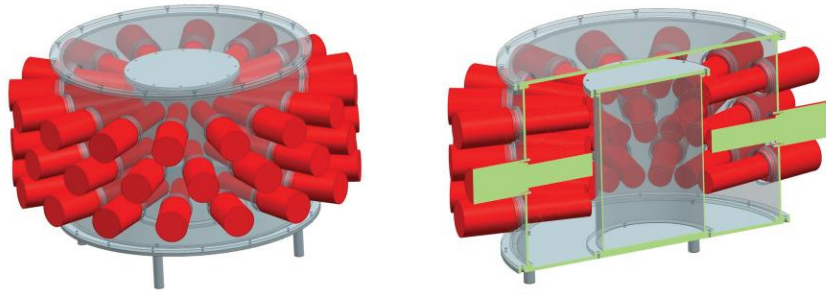

Figure 2.1: JUNO test facility setup in Legnaro.

The JUNO test facility recreates the Central Detector system and starting from the inside it is composed by an internal cylindrical vessel containing ∼17 l of liquid scintillator. The chosen materials are transparent Plexiglas for the vessel and a mixture of a solvent (LAB), Poly-Phenylene Oxide (PPO) and p-bis(o-MethylStyryl)-Benzene (bisMSB) for the liquid scintillator. The former component has a specific role, it is used as wavelength shifter in order to match the PMT response. The recipe of liquid scintillator is the same used in the Daya Bay neutrino experiment [6]. The JUNO test facility makes use of 48 Philips XP2020 PMTs with a diameter of about 5 cm. The signal is collected by 16 Global Control Units (GCU), each with three channels labelled 0, 1, 2. A photo of the whole apparatus is given in Fig. 2.2 where the PMTs voltage divider is clearly visible.

All PMTs photocathods are directed towards the inside of the vessel and they are arranged in three rings of 16 PMTs each and supported by a black plastic structure which surrounds the central vessel. The structure supports all PMTs and prevents external light from penetrating in the liquid scintillator vessel. There are 3 plastic scintillators with the purpose of detecting of muon from the cosmic rays and providing the trigger system. The first is set one on the top of the test facility, the second is located under the vessel, distant from the top plate ∼52 cm. The position of the last plastic scintillator is ∼3 cm below the
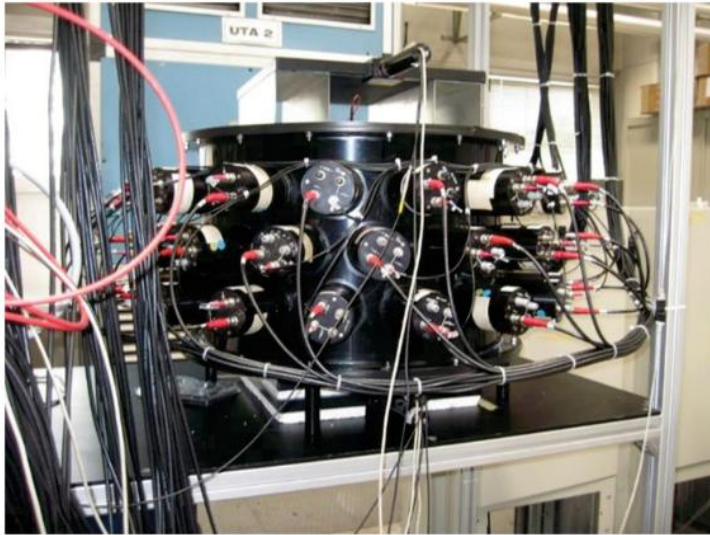
Figure 2.2: JUNO test facility.

second plate. They are together involved in the trigger system of the apparatus, giving a trigger signal if the AND coincidence is satisfied. The aim of the JUNO test facility is to study the JUNO readout electronics. Calibration tests are necessary for the purpose and now on-going. There are 39 out of 48 PMTs connected for this calibration test and 3 of them are either not working or give problems. In the following, data coming from different sources is considered:

- Collimated 137 Cs gamma source: the source is placed on the top of the setup and it is collimated by about 8 cm of lead;

- LED source: located on the top of the detector provides light at 405 nm and all parameters are set to work in single photon condition.

Chapter 3

PMT waveform charge reconstruction

In my thesis I firstly started reading and dealing with data coming from the integration
test facility at LNL saved in a ROOT TTree file. For this preliminary phase, I analyzed
data containing measurements of a 137 Cs source interacting with the liquid scintillator.
A typical reconstructed signal of one PMT channel, is a waveform in Fig. 3.1 where, in
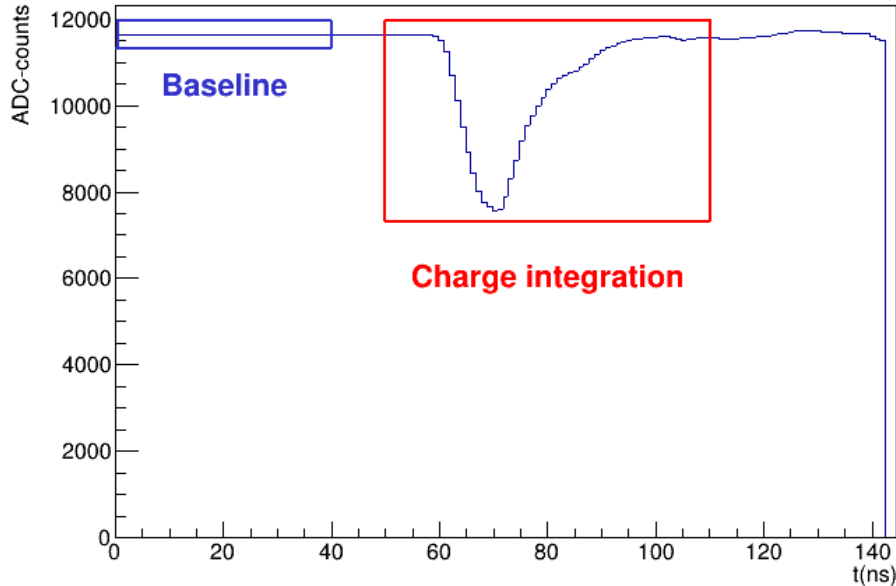the y axis, 1 ADC-count corresponds to 75 μV.

Figure 3.1: Typical waveform for 661 keV protons (Cs-137) interacting in the liquid scintillator.
The highlighted blue region shows the first 40 ns involved in the baseline calculation,
while the red area indicates the charge integration window.

The analysis of the signal starts from the determination of the baseline for each PMT, then
the reconstruction of the charge collected by a single PMT for each event is performed.

3.1   Baseline determination

In order to estimate the baseline for all the PMTs, the first 40 bins, corresponding to the
first 40 ns are considered; in this pre-trigger region, the mean value of the signal is taken
as baseline value. In Fig. 3.1 the region of the baseline calculation is highlighted in blue.
The oscillations are due to the electronic noise which is important to be characterized
and reduced as much as possible. Typical plot of baseline stability over time and of its
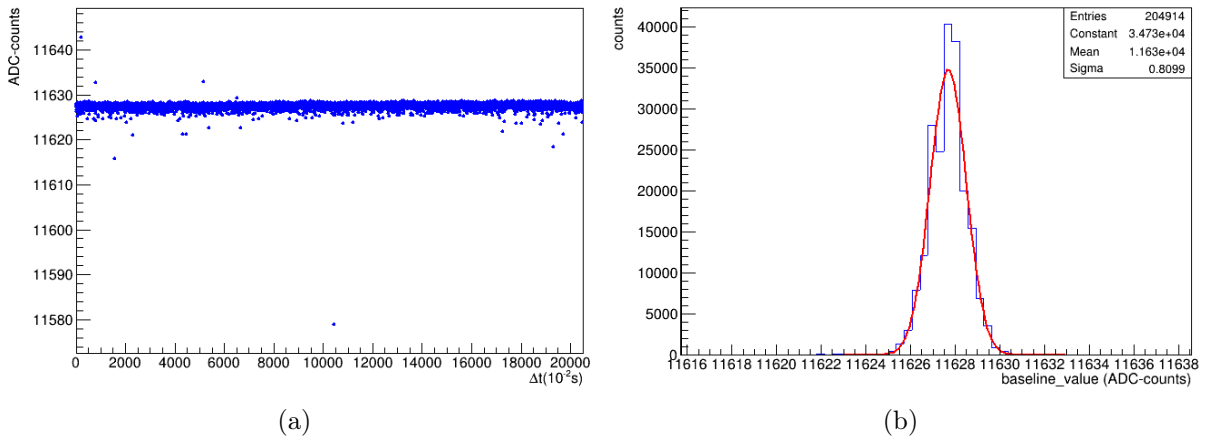dispersion can be seen in Fig. 3.2.

Figure 3.2: (a): Stability of the baseline over time. (b): Baseline values distribution. The result from a Gaussian fit is also shown in the same figure.

Looking at Fig. 3.2, the graph (a) shows the stability of the baseline over the whole data taking of ~5.5 minutes. Regarding the distribution of the baseline, the mean value is evaluated using a Gaussian fit and corresponds to $(1.16 \pm 0.81) \cdot 10^4$ ADC-counts. On the right side (b) of Fig. 3.2 is shown the distribution and the fit results. In particular, the dispersion can be estimated calculating the FWHM which corresponds to 150 μV. These numerical results are provided considering the specific shown analyzed data as example, since the baseline value can be arbitrarily set for the scope.

The same procedure has been used to calculate the baseline values of all events. In particular, for the LED source the first 60 bins, corresponding to the first 60 ns, has been chosen and it has been verified the stability of the baseline over the time for all 39 PMTs.

3.2 Charge reconstruction

The waveforms analysis provides an estimate of the baseline for every channel and for each event. This evaluation has great importance in order to reconstruct the charge acquired
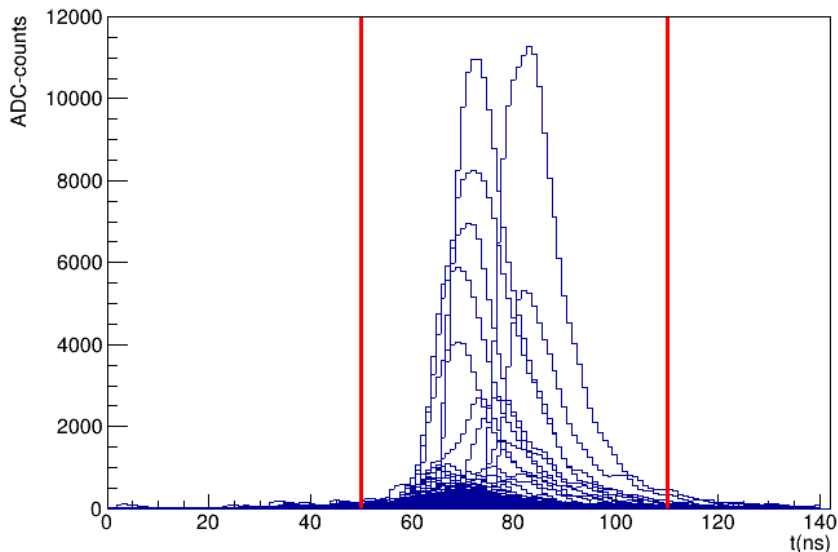

Figure 3.3: Signals of 1800 events are plotted in this image for determining the charge integration window.

by a PMT in a single event and further in the whole data taking. The charge is simply calculated as the integral of the current in a given time interval $Q = \int_{t_1}^{t_2} I\,dt$. Due to the necessity to convert the voltage signal into current it is provided a conversion factor equal to $1.5 \cdot 10^{-9}$ which takes into account the electronic input resistance of 50 Ω and the conversion 1 ADC-count = 75 μV. The charge value in μC collected by the PMT for each event can be found multiplying the total current by Δt. First of all, the waveform is subtracted form the baseline then the signal is integrated in a fixed region for all PMTs. Choosing a good integration window is crucial to obtain a good estimate for the charge. It must be sufficiently wide to integrate the entire signal and fairly general to match correctly signals of most of the events. A test has been made to choose the integration window for the 137Cs source from 50 ns to 110 ns which satisfies all requirements. The plot in Fig. 3.3 gives an immediate assessment of the signal position and width for more events considering a single channel.

In the end, it is possible to provide the distribution of the charge collected by a single PMT over the entire data taking in order to reconstruct the charge acquired by all PMTs. The obtained charge distribution for the 137 Cs source can been seen in Fig. 3.4.
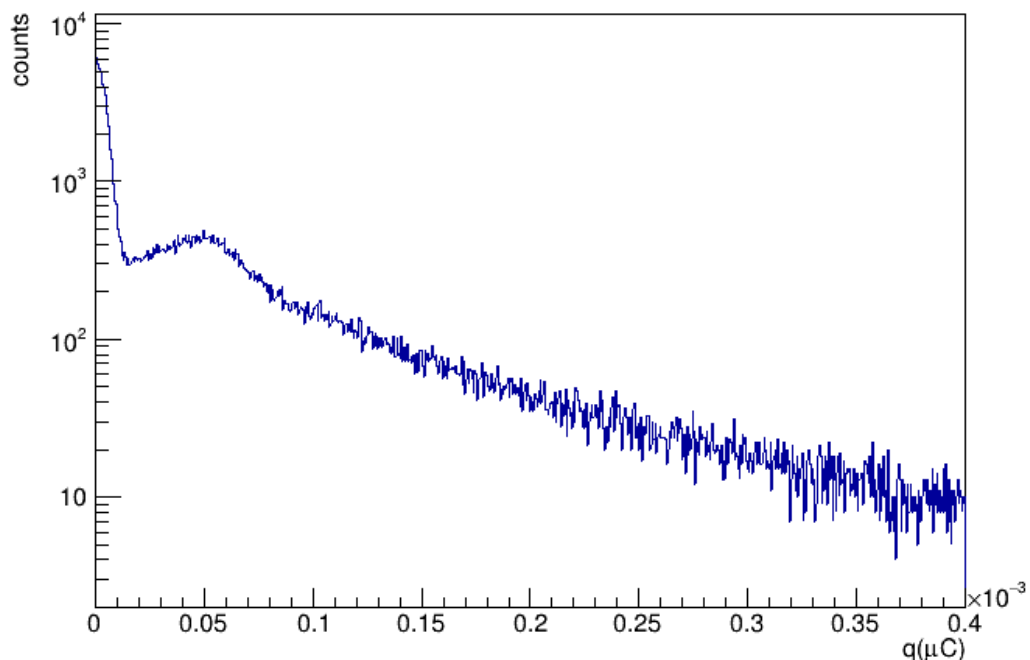

Figure 3.4: Example of charge reconstruction for the 137 Cs source.

Chapter 4

Single photon measurements and gain calculation

The main part of my thesis relates to the reconstruction of single photon signals produced by a LED source. The interest comes from the necessity of characterizing the electronic noise affecting the PMT response and of giving an estimate of the PMT gain. The experimental set up includes a LED providing light at 405 nm which is driven, through an optical fiber (Fig. 4.1), to the top of the vessel containing the liquid scintillator. The LED is connected to a pulse generator producing squared pulses with an amplitude of 6 V and 10 ns of width. The pulse generator, set with these specifics and with the implementation of an external trigger, generates pulses with a resulting rate of 500 Hz which are read as single photon signals from the detector. It must be specified that PMTs are not uniformly enlightened due to the position of the LED source.
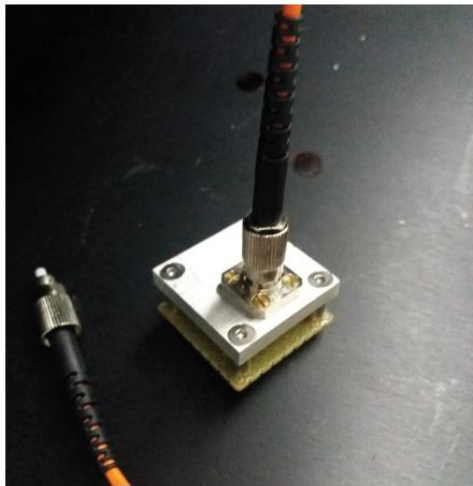
Figure 4.1: Photo of the set up for the LED source in which is visible the optical fiber used to lead the light to the top of the vessel.

The charge has been calculated following the procedures described in chapter 3 and an example of the characteristic charge distribution is given in Fig. 4.2.

4.1 Gain calculation and analysis

The calibration of the PMTs requires the study of gain evolution as a function of the PMT bias voltage. The aim is to use the same gain value by setting the corresponding voltages on all PMTs. Two peaks are evident looking at the charge spectrum and a third is hinted.

As can be seen from Fig. 4.2 the first peak, centered almost on zero, corresponds to the pedestal, while the second refers to the single photon signal, and the third relates to two-photon events. The characterization of single photon signal in the charge spectrum is an essential step on the gain determination since the latter is calculated as the difference between the mean value of the first peak μ_{pe1} and the mean value of the noise peak μ_n divided by the electron charge e.

$$G(\mu_n, \mu_{pe1}) = \frac{\mu_{pe1} - \mu_n}{e} \tag{4.1}$$

A triple Gaussian function has been used to fit the charge distribution in order to find the mean values of the two main peaks. The explicit shape of the function is:

$$F(x) = C_n \cdot e^{-\frac{(x-\mu_n)^2}{2\sigma_n^2}} + C_{pe1} \cdot e^{-\frac{(x-\mu_{pe1})^2}{2\sigma_{pe1}^2}} + C_{pe2} \cdot e^{-\frac{(x-2\mu_{pe1})^2}{4\sigma_n^2}} \tag{4.2}$$

Adding a third Gaussian to the fit is required to include the contribution given by two-photoelectron events. In particular it depends on σ_n and on μ_{pe1} as written in the equation 4.2. In Fig. 4.2 is shown the triple Gaussian fit of a LED source charge distribution histogram.
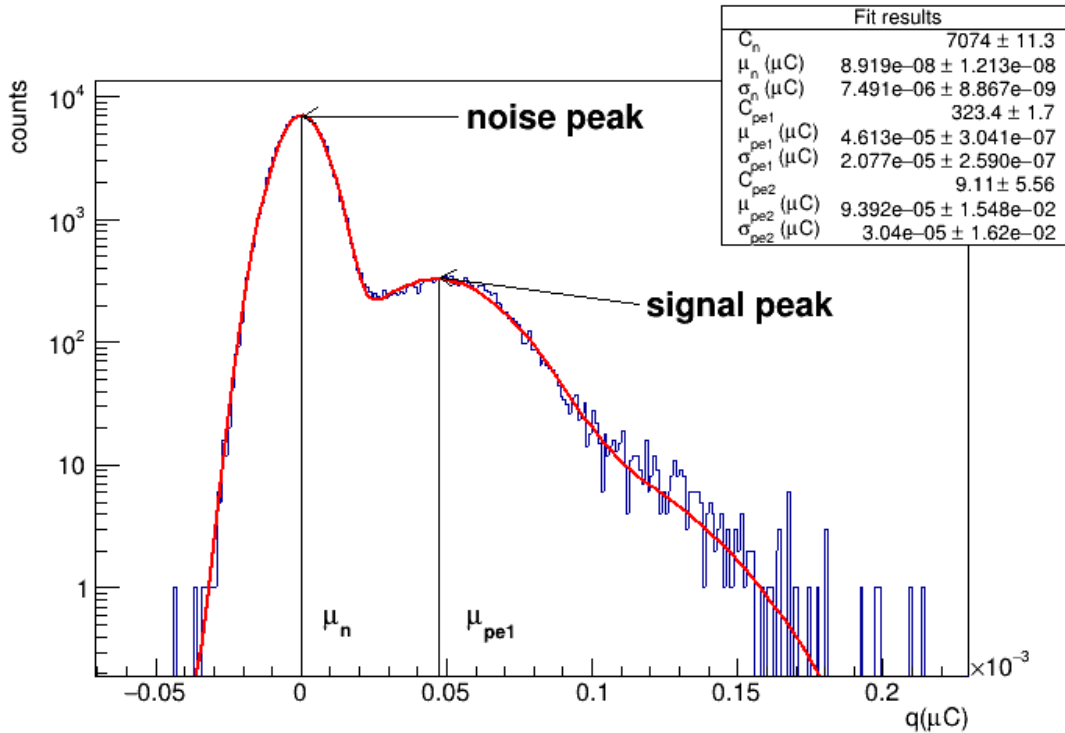
Figure 4.2: Charge distribution fitted with a triple Gaussian function. Noise peak and signal peak are indicated in the figure.

The initial photoelectron accelerated by a fixed voltage between dynodes (increasing the kinetic energy), creates avalanches of electrons multiplying the initial value of the electron charge to a final one depending on the gain value. A schematic view of the process for a standard PMT is illustrated in Fig. 4.3.

Studies on the gain can be performed varying the bias voltage in order to be able to work with a chosen gain adjusting the voltage for the scope. The charge spectrum changes as a function of the bias voltage variation is shown in Fig.4.4. Starting from the red distribution that does not resolve the single photon signal, the blue curve shows saturation
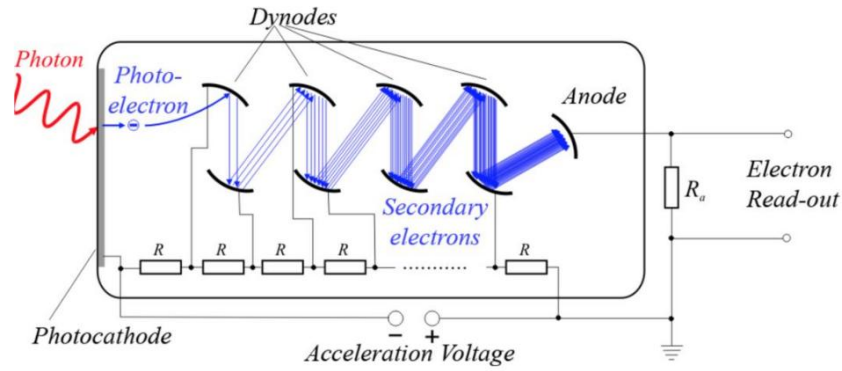
Figure 4.3: Working scheme of a photomultiplier (PMT) similar to those employed in the JUNO test facility.

phenomena that make it difficult to find the mean value of the signal peak by featuring a flat region on the top. The request is to well resolve the single photon peak and a gain around $2 \cdot 10^8$ seems to be a good value.
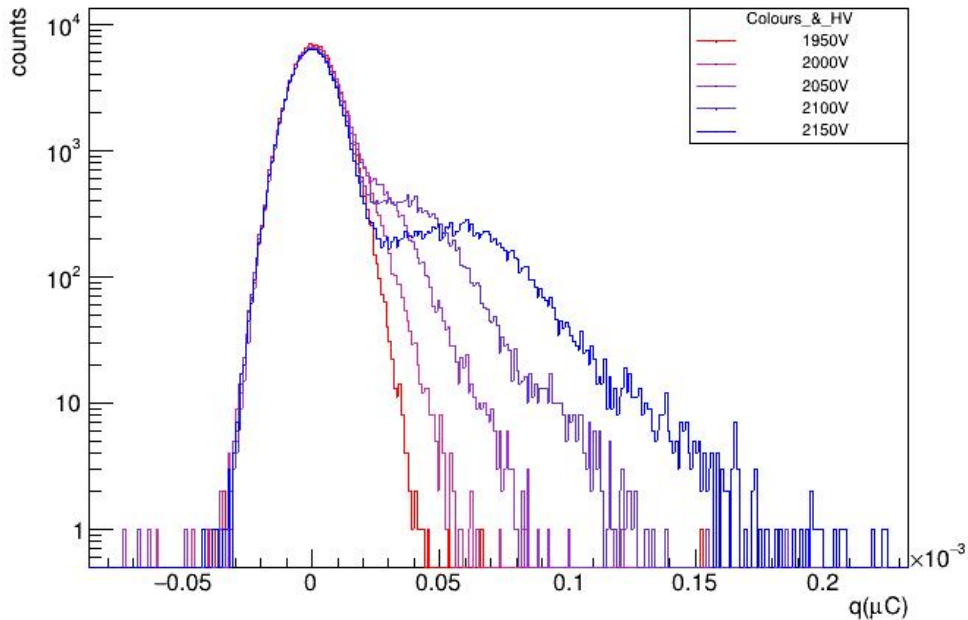
Figure 4.4: Visual description of the evolution of the charge distribution varying the voltage.

Measurements have been done varying the voltage from 1900 V to 2200 V and all gain values for each channel have been plotted in a graph. Two different fits have been performed to describe the trend of the data: an exponential and a second degree polynomial function. The uncertainties on the gain are calculated from the triple Gaussian fit by propagation. A study of the residuals has been done to verify the goodness of the fit. An example of the analysis can be found in Fig. 4.5, where the blue and red curves indicate the exponential and polynomial functions, respectively. Analysis results for all PMTs are given in the Appendix A.
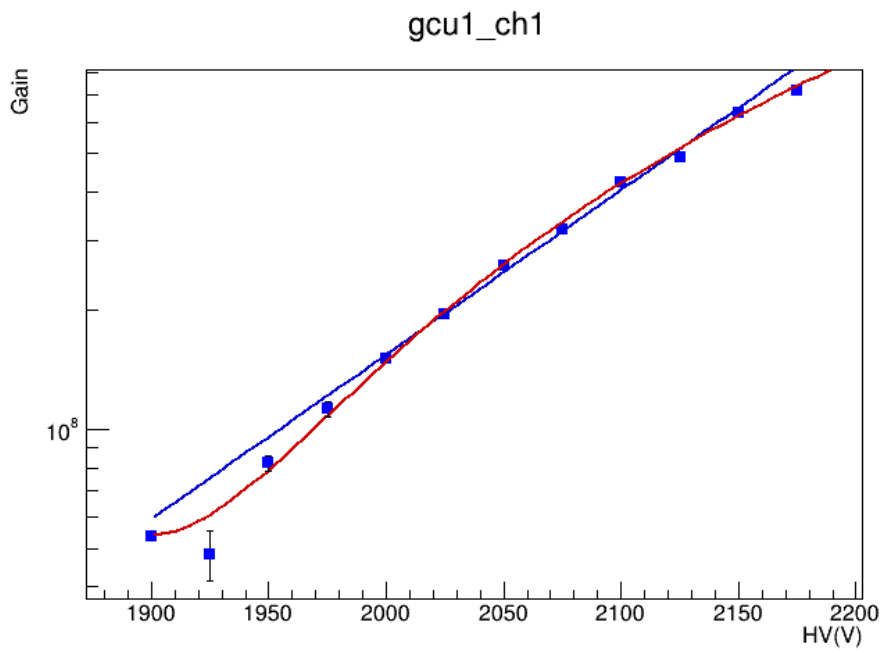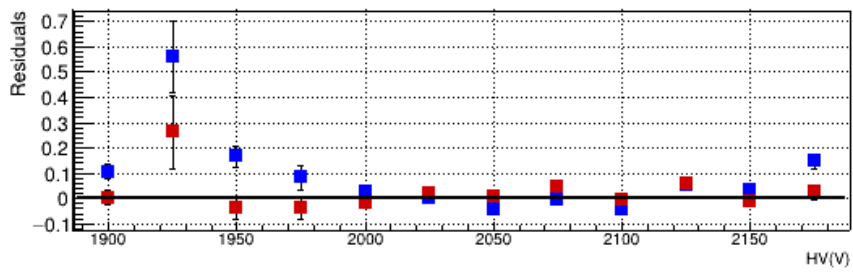
Figure 4.5: (a): Gain values as a function of high voltage. (b): Residual graph. The second degree polynomial fit is shown in red line, while the blue curve indicates the exponential fit.

Chapter 5

Conclusions

In this thesis, studies on PMTs responses have been performed for calibration operations of the 39 PMTs installed on the JUNO test facility at LNL. A procedure for the charge reconstruction from waveform signals has been developed and studies has been conducted on single photon signal from LED source, including gain calculations and analysis. The procedure has been tested with 137 Cs photons data and the charge has been reconstructed with simple integration of the PMT waveform. Studies on the baseline stability over the time and on its dispersion have been performed. In the second part of the thesis, LED generated photons signals in single photon condition have been studied in order to characterize PMTs responses and provide estimates of the PMT gain values varying the bias voltage of the PMTs. The charge has been reconstructed following the abovementioned procedure setting parameters for the scope. A triple Gaussian function has been used to fit the distribution in order to find the positions of peaks and subsequently calculate the gain. Analysis of the gain variation to voltage change has been performed for all PMTs and gain values have been fitted with two different functions: an exponential and a second-degree polynomial. Using fits results, it has been possible to find the bias voltage value for every PMT corresponding to a gain of $2 \cdot 10^8$. This value has been chosen to satisfy the request to well resolve the single photon peak.

Appendix A

Detailed results for LED single photon measurements

This section collects all the results from the analysis of the LED single photon measurements. In particular Tab. A.1 presents in the second and third columns the voltage values to set in order to work with a gain of $2 \cdot 10^8$. These values are calculated for each PMT using an exponential function and a second degree polynomial. Fig A.1 and Fig. A.2 are a collection of histograms representing all PMTs charge spectrum fitted with a triple Gaussian function. Fit results are provided in Tab. A.2, A.3, A.4. Finally, it is possible to find in Fig. A.3, A.4 and A.5 all the graphs "Gain vs HV" with their residual graphs below.

Gain analysis		
PMT	HV from exponential fit [V]	HV from polynomial fit [V]
GCU 1 CH 1	2027	2025
GCU 1 CH 2	2116	2108
GCU 2 CH 0	2028	2019
GCU 2 CH 1	2070	2057
GCU 3 CH 0	2045	2035
GCU 3 CH 1	1945	1951
GCU 3 CH 2	1995	1987
GCU 4 CH 0	2057	2041
GCU 4 CH 1	1997	2002
GCU 5 CH 0	1965	1965
GCU 5 CH 1	2183	2185
GCU 5 CH 2	2144	2140
GCU 6 CH 0	2119	2112
GCU 6 CH 1	2131	2122
GCU 6 CH 2	1946	1958
GCU 7 CH 0	2020	2016
GCU 7 CH 1	2057	2054
GCU 7 CH 2	2177	2178
GCU 8 CH 0	2123	2111
GCU 8 CH 1	2010	2004
GCU 8 CH 2	1963	1975
GCU 9 CH 0	2091	2076
GCU 9 CH 1	2082	2069
GCU 9 CH 2	2044	2032
GCU 10 CH 0	2099	2071
GCU 10 CH 1	2113	2091
GCU 10 CH 2	2000	1995
GCU 11 CH 0	2117	2103
GCU 11 CH 1	1977	1981
GCU 11 CH 2	1913	1920
GCU 12 CH 0	1956	1967
GCU 12 CH 1	2073	2041
GCU 12 CH 2	2117	2104
GCU 13 CH 0	2122	2119
GCU 13 CH 1	2050	2039
GCU 13 CH 2	2048	2033

Table A.1: Summary table of gain calculation results.
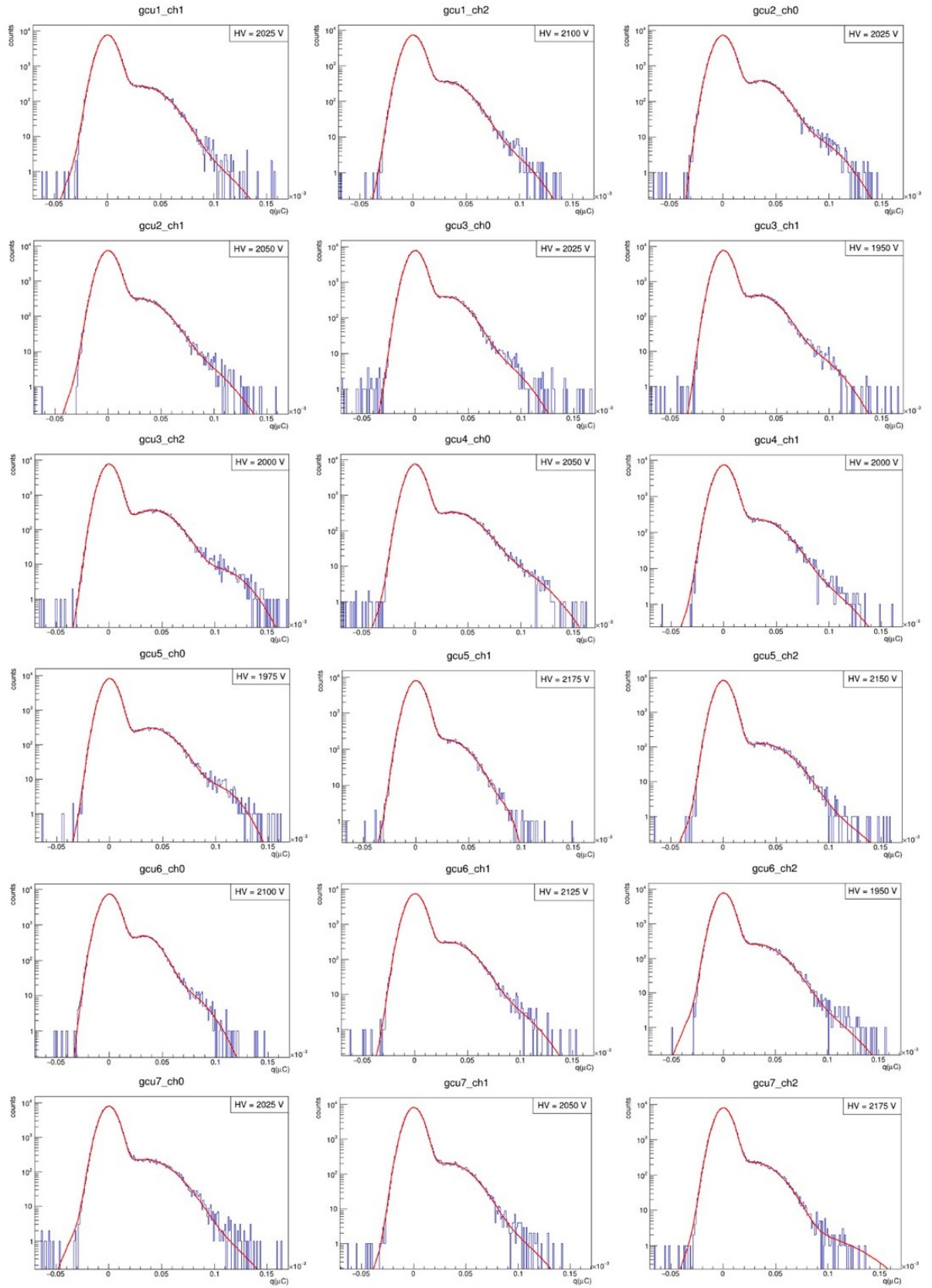
Figure A.1: Charge spectrum for LED source with a PMT gain about $2 \cdot 10^8$ and triple Gaussian fit.
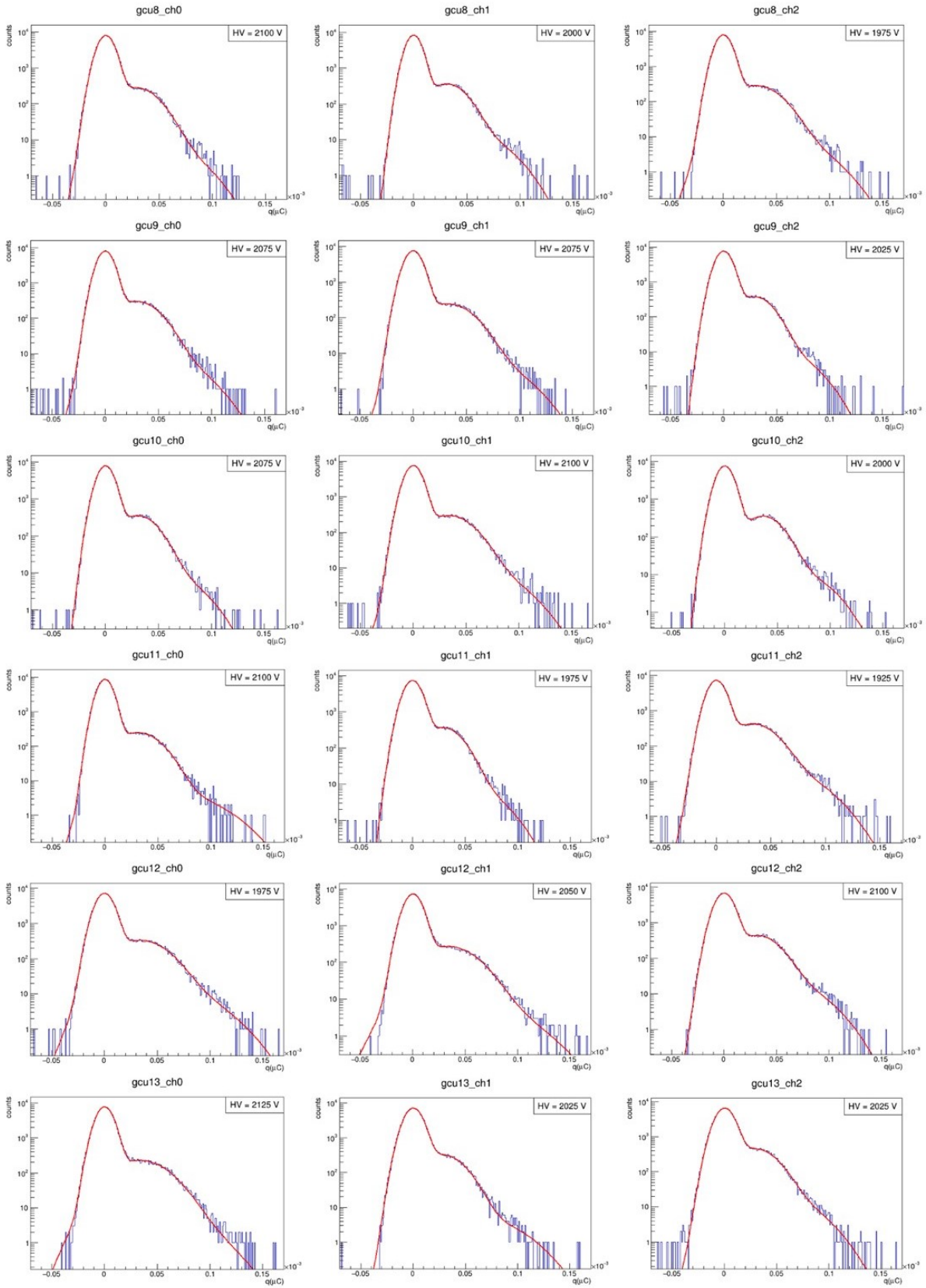
Figure A.2: Charge spectrum for LED source with a PMT gain about $2 \cdot 10^8$ and triple Gaussian fit.

Triple Gaussian fit results - noise peak				
PMT	HV [V]	C_n [10^3counts]	μ_n [$10^{-7}\mu$C]	σ_n [$10^{-6}\mu$C]
GCU 1 CH 1	2025	7.62 ± 0.01	1.1 ± 0.1	7.192 ± 0.008
GCU 1 CH 2	2100	7.18 ± 0.01	0.9 ± 0.1	7.462 ± 0.007
GCU 2 CH 0	2025	7.15 ± 0.01	0.7 ± 0.1	7.529 ± 0.008
GCU 2 CH 1	2050	7.47 ± 0.01	1.0 ± 0.1	7.234 ± 0.007
GCU 3 CH 0	2025	7.72 ± 0.01	0.1 ± 0.09	6.940 ± 0.006
GCU 3 CH 1	1950	7.69 ± 0.01	1 ± 0.1	6.911 ± 0.006
GCU 3 CH 2	2000	7.75 ± 0.01	1.2 ± 0.1	6.847 ± 0.007
GCU 4 CH 0	2050	7.50 ± 0.03	0.6 ± 0.1	6.706 ± 0.006
GCU 4 CH 1	2000	7.46 ± 0.01	0.8 ± 0.1	7.438 ± 0.008
GCU 5 CH 0	1975	8.30 ± 0.01	0.6 ± 0.2	6.70 ± 0.02
GCU 5 CH 1	2175	7.99 ± 0.03	1.3 ± 0.2	7.10 ± 0.02
GCU 5 CH 2	2150	8.28 ± 0.01	0.8 ± 0.1	6.906 ± 0.008
GCU 6 CH 0	2100	7.37 ± 0.03	1.5 ± 0.3	7.26 ± 0.02
GCU 6 CH 1	2125	7.49 ± 0.01	1.1 ± 0.1	7.260 ± 0.008
GCU 6 CH 2	1950	7.79 ± 0.01	1.6 ± 0.1	7.053 ± 0.006
GCU 7 CH 0	2025	7.91 ± 0.01	0.9 ± 0.1	6.972 ± 0.008
GCU 7 CH 1	2050	8.17 ± 0.01	1.3 ± 0.1	7.072 ± 0.007
GCU 7 CH 2	2175	7.92 ± 0.03	1.5 ± 0.2	7.03 ± 0.02
GCU 8 CH 0	2100	7.9 ± 0.01	1.1 ± 0.1	7.004 ± 0.008
GCU 8 CH 1	2000	8.33 ± 0.01	0.6 ± 0.1	6.522 ± 0.007
GCU 8 CH 2	1975	7.83 ± 0.01	1.0 ± 0.1	6.964 ± 0.007
GCU 9 CH 0	2075	8.07 ± 0.01	0.3 ± 0.1	6.772 ± 0.006
GCU 9 CH 1	2075	7.46 ± 0.01	1.9 ± 0.1	7.404 ± 0.009
GCU 9 CH 2	2025	7.67 ± 0.01	0.5 ± 0.1	7.095 ± 0.007
GCU 10 CH 0	2075	7.86 ± 0.01	0.5 ± 0.1	6.937 ± 0.007
GCU 10 CH 1	2100	7.54 ± 0.01	0.6 ± 0.1	7.194 ± 0.008
GCU 10 CH 2	2000	7.56 ± 0.03	1.5 ± 0.2	7.20 ± 0.02
GCU 11 CH 0	2100	8.6 ± 0.03	0.7 ± 0.2	6.45 ± 0.01
GCU 11 CH 1	1975	7.35 ± 0.01	0.2 ± 0.1	7.422 ± 0.008
GCU 11 CH 2	1925	7.306 ± 0.009	0.5 ± 0.1	7.167 ± 0.006
GCU 12 CH 0	1975	7.05 ± 0.01	0.7 ± 0.1	7.512 ± 0.007
GCU 12 CH 1	2050	7.14 ± 0.01	1.8 ± 0.1	7.526 ± 0.006
GCU 12 CH 2	2100	6.749 ± 0.009	1.1 ± 0.1	7.730 ± 0.009
GCU 13 CH 0	2125	7.7 ± 0.1	0.79 ± 0.09	7.102 ± 0.006
GCU 13 CH 1	2025	7.06 ± 0.02	1.4 ± 0.3	7.72 ± 0.02
GCU 13 CH 2	2025	6.460 ± 0.008	0.9 ± 0.1	8.024 ± 0.007

Table A.2: Fit results for the noise peak (first peak) of the triple Gaussian fit.

Triple Gaussian fit results - single photon signal peak				
PMT	HV [V]	C_{pe1} [10^2counts]	μ_{pe1} [$10^{-5}\mu$C]	σ_{pe1} [$10^{-5}\mu$C]
GCU 1 CH 1	2025	2.64 ± 0.03	3.14 ± 0.05	1.96 ± 0.03
GCU 1 CH 2	2100	3.54 ± 0.02	3.07 ± 0.03	1.77 ± 0.02
GCU 2 CH 0	2025	3.70 ± 0.02	3.56 ± 0.02	1.61 ± 0.02
GCU 2 CH 1	2050	3.10 ± 0.03	2.96 ± 0.03	1.86 ± 0.02
GCU 3 CH 0	2025	3.88 ± 0.02	2.92 ± 0.02	1.62 ± 0.01
GCU 3 CH 1	1950	4.00 ± 0.02	3.28 ± 0.02	1.65 ± 0.02
GCU 3 CH 2	2000	3.61 ± 0.02	3.96 ± 0.02	1.83 ± 0.02
GCU 4 CH 0	2050	3.30 ± 0.07	3.57 ± 0.04	1.96 ± 0.04
GCU 4 CH 1	2000	2.24 ± 0.02	3.25 ± 0.05	1.97 ± 0.03
GCU 5 CH 0	1975	3.03 ± 0.01	3.76 ± 0.03	1.87 ± 0.02
GCU 5 CH 1	2175	1.83 ± 0.03	2.88 ± 0.07	1.78 ± 0.04
GCU 5 CH 2	2150	1.25 ± 0.02	3.59 ± 0.08	2.13 ± 0.03
GCU 6 CH 0	2100	4.79 ± 0.09	3.21 ± 0.03	1.31 ± 0.04
GCU 6 CH 1	2125	3.06 ± 0.02	3.29 ± 0.03	1.80 ± 0.03
GCU 6 CH 2	1950	2.50 ± 0.02	3.12 ± 0.04	2.05 ± 0.02
GCU 7 CH 0	2025	2.24 ± 0.02	3.42 ± 0.06	2.15 ± 0.02
GCU 7 CH 1	2050	2.04 ± 0.02	3.20 ± 0.06	1.89 ± 0.03
GCU 7 CH 2	2175	2.25 ± 0.03	2.98 ± 0.05	1.90 ± 0.03
GCU 8 CH 0	2100	2.75 ± 0.03	2.90 ± 0.04	1.70 ± 0.03
GCU 8 CH 1	2000	3.59 ± 0.02	3.12 ± 0.02	1.54 ± 0.02
GCU 8 CH 2	1975	2.80 ± 0.02	3.16 ± 0.04	1.90 ± 0.02
GCU 9 CH 0	2075	2.98 ± 0.02	2.98 ± 0.03	1.74 ± 0.02
GCU 9 CH 1	2075	2.41 ± 0.02	3.36 ± 0.05	1.91 ± 0.03
GCU 9 CH 2	2025	3.74 ± 0.02	2.91 ± 0.02	1.45 ± 0.02
GCU 10 CH 0	2075	3.49 ± 0.02	3.09 ± 0.02	1.54 ± 0.02
GCU 10 CH 1	2100	2.94 ± 0.02	3.39 ± 0.03	1.89 ± 0.03
GCU 10 CH 2	2000	3.58 ± 0.05	3.68 ± 0.03	1.50 ± 0.04
GCU 11 CH 0	2100	2.45 ± 0.03	3.17 ± 0.04	1.78 ± 0.03
GCU 11 CH 1	1975	3.61 ± 0.03	2.94 ± 0.02	1.49 ± 0.02
GCU 11 CH 2	1925	4.18 ± 0.02	3.31 ± 0.02	1.77 ± 0.02
GCU 12 CH 0	1975	3.22 ± 0.02	3.45 ± 0.04	2.10 ± 0.02
GCU 12 CH 1	2050	2.61 ± 0.03	3.44 ± 0.04	2.21 ± 0.02
GCU 12 CH 2	2100	4.28 ± 0.02	3.19 ± 0.02	1.73 ± 0.02
GCU 13 CH 0	2125	2.24 ± 0.02	3.41 ± 0.04	2.19 ± 0.01
GCU 13 CH 1	2025	3.17 ± 0.05	2.87 ± 0.05	1.68 ± 0.04
GCU 13 CH 2	2025	4.45 ± 0.02	2.92 ± 0.02	1.73 ± 0.01

Table A.3: Fit results for the single photon signal peak (second peak) of the triple Gaussian fit.

Triple Gaussian fit results - two-photon signal peak				
PMT	HV [V]	C_{pe2} [counts]	$10^{-2}\mu_{pe2}$ [μC]	σ_{pe2} [$10^{-2}\mu$C]
GCU 1 CH 1	2025	4 ± 6	0.006 ± 3	0.003 ± 3
GCU 1 CH 2	2100	8 ± 6	0.006 ± 2	0.003 ± 0.01
GCU 2 CH 0	2025	11 ± 7	0.007 ± 1	0.002 ± 1
GCU 2 CH 1	2050	9 ± 7	0.006 ± 1	0.003 ± 1
GCU 3 CH 0	2025	10 ± 6	0.006	0.002 ± 0.009
GCU 3 CH 1	1950	1 ± 7	0.007 ± 1	0.002 ± 0.01
GCU 3 CH 2	2000	10 ± 6	0.008 ± 1	0.003 ± 1
GCU 4 CH 0	2050	12 ± 5	0.007 ± 0.002	0.0028 ± 0.0006
GCU 4 CH 1	2000	6 ± 5	0.006 ± 2	0.005 ± 2
GCU 5 CH 0	1975	9 ± 6	0.008 ± 2	0.003 ± 0.01
GCU 5 CH 1	2175	1.6 ± 0.8	0.0083 ± 0.0004	0.0007 ± 0.0005
GCU 5 CH 2	2150	2 ± 4	0.006 ± 0.4	0.003 ± 0.02
GCU 6 CH 0	2100	14 ± 5	0.006 ± 0.001	0.0019 ± 0.0006
GCU 6 CH 1	2125	7 ± 6	0.007 ± 2	0.003 ± 0.01
GCU 6 CH 2	1950	5 ± 6	0.006 ± 2	0.003 ± 3
GCU 7 CH 0	2025	3 ± 6	0.007 ± 0.3	0.003 ± 0.01
GCU 7 CH 1	2050	3 ± 6	0.005 ± 3	0.003 ± 4
GCU 7 CH 2	2175	1.9 ± 0.7	0.008 ± 0.002	0.004 ± 0.001
GCU 8 CH 0	2100	5 ± 6	0.006 ± 2	0.002 ± 3
GCU 8 CH 1	2000	10 ± 7	0.006 ± 1	0.002 ± 1
GCU 8 CH 2	1975	6 ± 6	0.006 ± 2	0.003 ± 2
GCU 9 CH 0	2075	6 ± 6	0.006 ± 2	0.003 ± 2
GCU 9 CH 1	2075	5 ± 6	0.007 ± 2	0.003 ± 3
GCU 9 CH 2	2025	8 ± 7	0.006 ± 1	0.002 ± 1
GCU 10 CH 0	2075	7 ± 6	0.006 ± 2	0.002 ± 0.01
GCU 10 CH 1	2100	6 ± 6	0.007 ± 2	0.003 ± 2
GCU 10 CH 2	2000	10 ± 3	0.008 ± 0.001	0.0020 ± 0.0007
GCU 11 CH 0	2100	3 ± 1	0.007 ± 0.001	0.0030 ± 0.0006
GCU 11 CH 1	1975	6 ± 6	0.006 ± 2	0.002 ± 2
GCU 11 CH 2	1925	14 ± 7	0.007 ± 1	0.003 ± 0.007
GCU 12 CH 0	1975	10 ± 6	0.007 ± 1	0.003 ± 1
GCU 12 CH 1	2050	8 ± 7	0.005 ± 0.5	0.004 ± 0.005
GCU 12 CH 2	2100	15 ± 7	0.007 ± 1	0.003 ± 0.008
GCU 13 CH 0	2125	5 ± 6	0.006 ± 0.3	0.003 ± 0.006
GCU 13 CH 1	2025	4 ± 1	0.007 ± 0.001	0.0030 ± 0.0007
GCU 13 CH 2	2025	14 ± 7	0.006 ± 1	0.003 ± 0.007

Table A.4: Fit results for the two-photon signal peak (third peak) of the triple Gaussian fit.
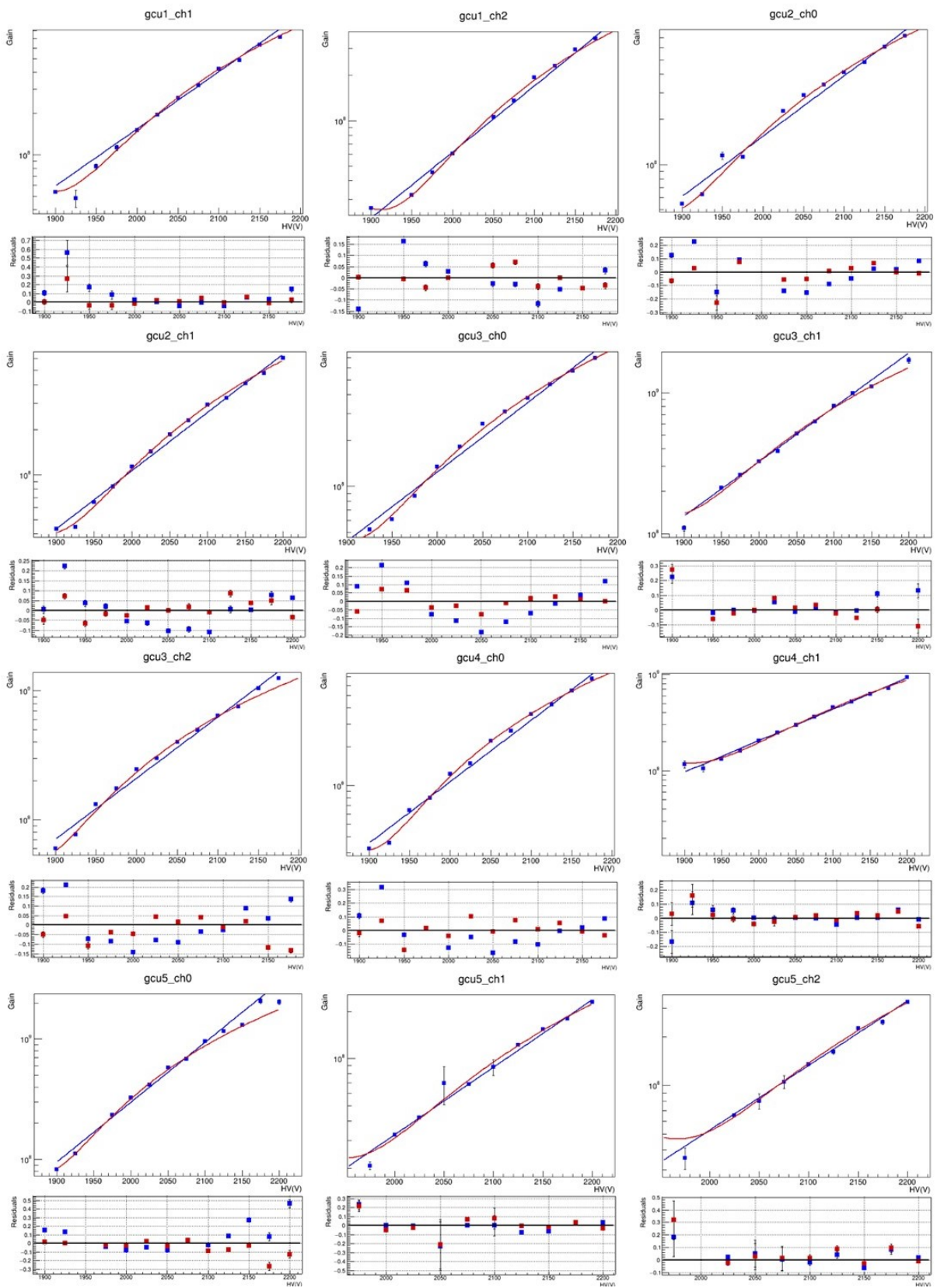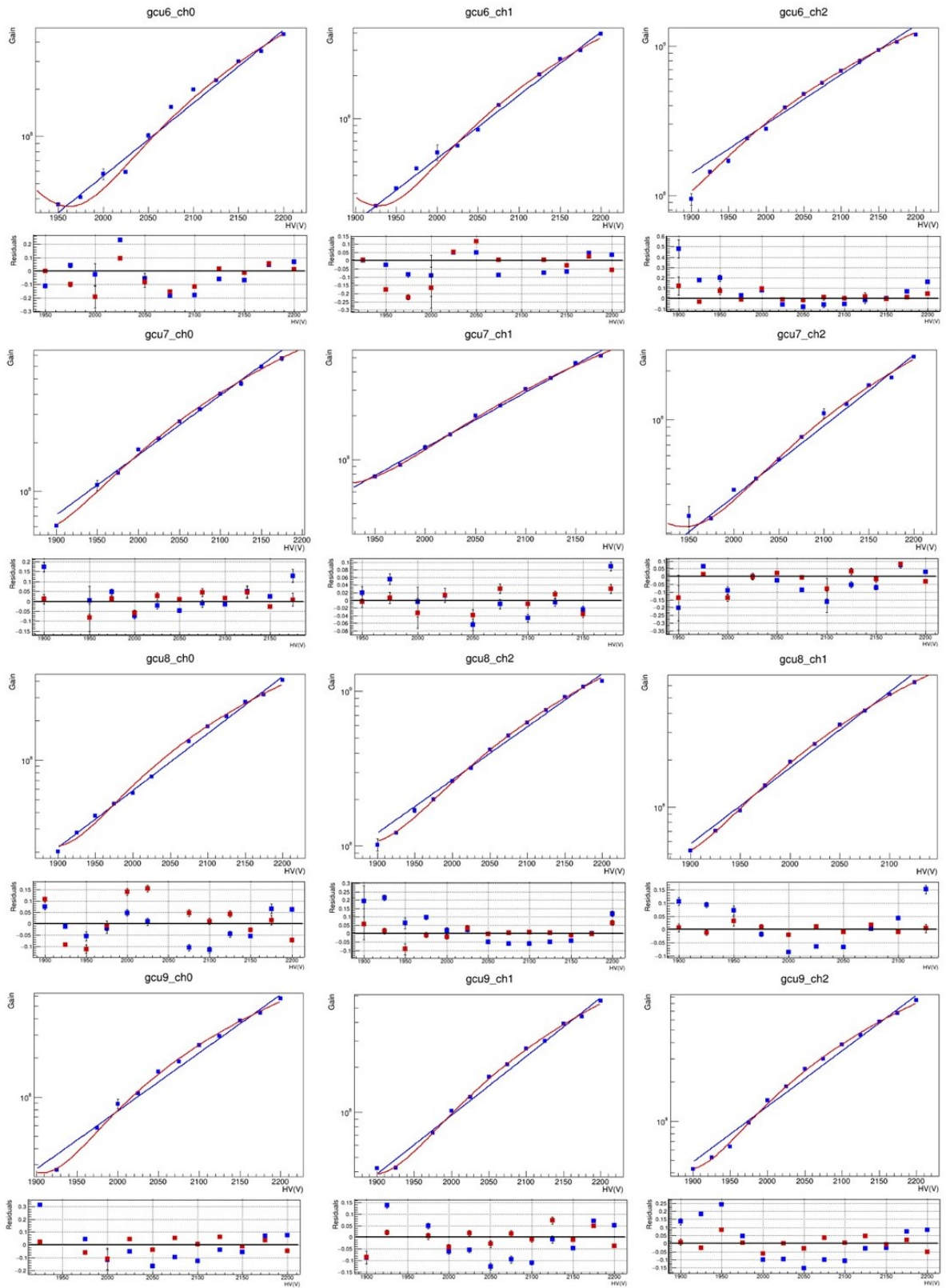
Figure A.3: "Gain vs HV" and residual graphs.

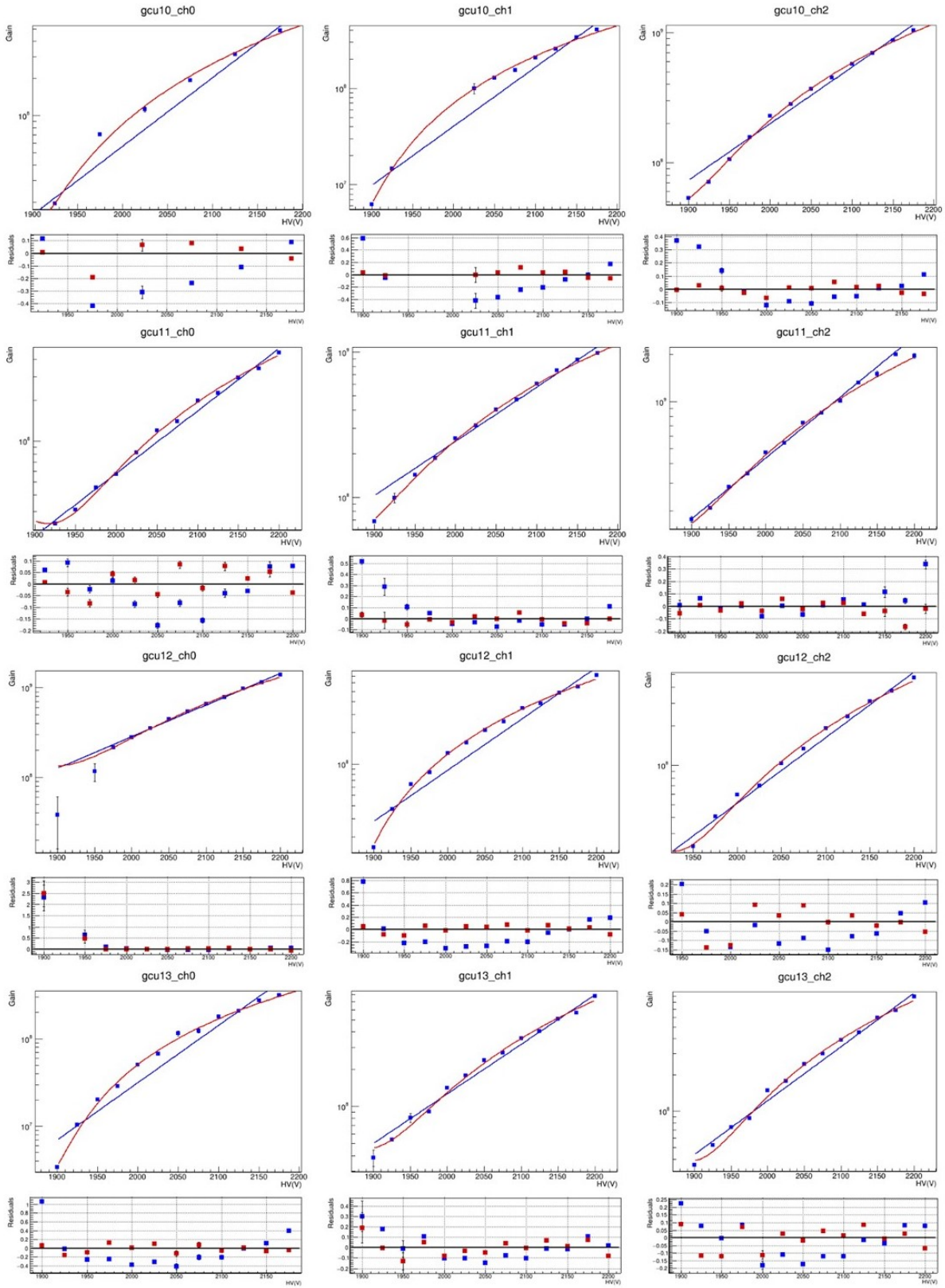**Figure A.4:** "Gain vs HV" and residual graphs.

Figure A.5: "Gain vs HV" and residual graphs.

Bibliography

[1] An Fengpeng et al., *Neutrino Physics with JUNO*, J. Phys. G43 (2016), 030401.

[2] A. Abusleme et al., *TAO Conceptual Design Report*, arXiv 2005.08745, May 2020.

[3] X. Qian and P. Vogel, *Neutrino mass hierarchy*, Progr. Part. Nucl. Phys 83(2015)1.

[4] B. Pontecorvo, Sov. Phys. JETP 6(1957)429.
Z. Maki, M. Nakagawa and S. Sakota, Progr. th. Phys. 28(1962)870.

[5] A. Abusleme et al., *Calibration Strategy of the JUNO experiment*, JHEP 03 (2001) 004.

[6] A. Abusleme et al., *Optimization of the JUNO liquid scintillator composition using a Daya Bay antineutrino detector*, Nucl.Instr. Meth. A 988 (2021) 164823.